Enhanced Power Conversion Efficiency in Solution-Processed Rigid CuIn(S,Se)$_2$ and Flexible Cu(In,Ga)Se$_2$ Solar Cells Utilizing Plasmonic Au-SiO$_2$ Core-Shell Nanoparticles

Chia-Wei Chen, Yi-Ju Chen, Stuart R. Thomas, Yu-Ting Yen, Lung-Teng Cheng, Yi-Chung Wang, Teng-Yu Su, Hao Lin, Cheng-Hung Hsu, Johnny C. Ho, Tung-Po Hsieh,* and Yu-Lun Chueh*

Plasmonic resonance effect triggered by gold nanoparticles (NPs) is utilized to enhance light harvesting in different types of thin-film solar cells. However, there is no report using the plasmonic resonance effect triggered by metal NPs in chalcopyrite absorber-based devices because of the high reactivity between the metal NPs and indium/copper/gallium during the required high-temperature selenization process. In this work, Au NPs encapsulated by a thin protective silicon oxide shell in the chalcopyrite absorber-based solar cells deposited by scalable solution deposition techniques under the 600 °C selenization process are demonstrated. The increased scattering and surface plasmonic resonance induced field generated by the nanoparticles can lead to significant enhancement in light absorption and charge carrier generation across a broad spectral range. Enhanced power conversion efficiency in solution-processed rigid CuIn(S,Se)$_2$ from 1.95 to 2.26% and flexible Cu(In,Ga)Se$_2$ solar cells from 9.28% to 10.88% is achieved after the addition of plasmonic Au-SiO$_2$ core-shell NPs in the absorber layer. This work demonstrates a facile method for chalcopyrite solar cell enhancement, which is compatible with low-cost and high-throughput manufacturing process.

1. Introduction

Nanoscale metal particles and structures are now widely utilized as a method to enhance light harvesting by the plasmonic effect that can trap and guide light at the sub-wavelength scale.[1–3] The plasmonic effect has been applied in numerous fields, including solar cells, optical coatings, bio-applications, and a host of other spectroscopic related applications.[1,4–8] Among metal NPs, Au and Ag have commonly used elements for plasmonic solar cell applications due to the favorably plasmonic absorption behavior within the solar spectrum region and also the chemical stability.[2,3,5,9–11] To date, plasmonic NPs have now been incorporated into a variety of light absorbing materials and have been successfully demonstrated in organic photovoltaic devices (OPVs),[10,12–15] dye-sensitized solar cells (DSSCs),[16–18] and other thin-film silicon solar cells.[2,19–21]

It is well-known that chalcopyrite-based solar cells are currently one of the most promising thin-film technologies for renewable energy and the significant effort has been placed on developing low-cost fabrication methods in the

C. W. Chen, Y. J. Chen, Dr. S. R. Thomas, Dr. Y. T. Yen, Dr. Y. C. Wang, T. Y. Su, C. H. Hsu, Prof. Y. L. Chueh
Department of Materials Science and Engineering, and Frontier Research Center on Fundamental and Applied Sciences of Matters
National Tsing Hua University
Hsinchu 30013 Taiwan, ROC
Email: ylchueh@mx.nthu.edu.tw

C. W. Chen, Y. J. Chen, Dr. S. R. Thomas, Dr. Y. T. Yen, Dr. Y. C. Wang, T. Y. Su, C. H. Hsu, Prof. Y. L. Chueh
Department of Physics
National Sun Yat-sen University
Kaohsiung 80424 Taiwan, ROC

Dr. L. T. Cheng, Dr. T. P. Hsieh
Green Energy & Environment Research Laboratory
Industrial Technology Research Institute
Hsinchu 31040, Taiwan
E-mail: TP@itri.org.tw

H. Lin, Prof. J. C. Ho
Department of Materials Science and Engineering
City University of Hong Kong
Hong Kong 999077, P. R. China

novel and flexible applications.[22–24] Chalcopyrite-based solar cells demonstrated by Solar Frontier in Japan have achieved a power conversion efficiency (PCE) as high as 22.9%, the highest efficiency for any thin-film solar cell to date.[25] Typically, NP-based plasmonic-enhanced photovoltaic devices can increase light absorption by two mechanisms. First, the NPs acting as scattering elements can effectively increase the optical path length, and therefore increase the probability of photon absorption. Second, surface plasmon resonances (SPR) at the NP surface can trigger the plasmonic-induced near-field, which effectively increases the absorption cross-section.[26] However, the demonstration of the plasmonic-enhanced chalcopyrite ($CuIn(S,Se)_2$, $Cu(In,Ga)Se_2$) solar cells by plasmonic NPs remains a significant challenge due to the high reactivity of plasmonic NPs with chalcopyrite films, resulting in the formation of unwanted phases and poor stoichiometry with poor device performance. For example, Au NPs will chemically react with In/Cu/Ga at the selenization temperature of $>400\,°C$.

In this regard, we, for the first time, demonstrated the synthesis of Au-SiO$_2$ core-shell NPs ($Au@SiO_2$ NPs) and its application as a plasmonic enhancer and scattering element in high-performance chalcopyrite solar cells. The work here focuses primarily on the development of solution processed $CuIn(S,Se)_2$ based solar cells on rigid substrates. Additionally, we have demonstrated the broader suitability of our $Au@SiO_2$ NPs in chalcopyrite solar cells by solution processed $Cu(In,Ga)Se_2$ flexible solar cells. The SiO_2 shell provides an essential encapsulation layer that prevents any reaction between the Au and In/Cu/Ga within the absorber layer during the high-temperature selenization process. Our $Au@SiO_2$ NPs were combined with $CuIn(S,Se)_2$ and $Cu(In,Ga)Se_2$ NPs in the solution followed by drop-casting and inkjet printing to prepare rigid $CuIn(S,Se)_2$ and flexible $Cu(In,Ga)Se_2$ devices, respectively. The SiO_2 shell thickness and structural properties of the Au and $Au@SiO_2$ NPs, as well as the thermal stability of the $Au@SiO_2$ NPs, were characterized in detail. X-ray diffraction (XRD) and scanning electron microscopy (SEM) analysis were used to ensure no degradation in the quality of the absorber layer after the addition of $Au@SiO_2$ NPs. The effects of different thicknesses of the SiO_2 shell layer were assessed by ultraviolet (UV)–visible (Vis) spectroscopy while the influence of the pre-deposition (in solution) ratio between $Au@SiO_2$ NPs and the $CuInS_2$ precursor to film formation was investigated. By optimizing the concentration and shell size of the $Au@SiO_2$ NPs, a significant enhancement in device performance for both rigid $CuIn(S,Se)_2$ (1.95–2.26%) and flexible $Cu(In,Ga)Se_2$ (9.28–10.88%) solar cells can be achieved. We believe that this achievement demonstrates a highly promising method for the enhancement of power conversion efficiencies in chalcopyrite based thin-film solar cells.

2. Results and Discussion

2.1. Plasmonic Enhanced $Au@SiO_2$-$CuIn(S,Se)_2$ Solar Cells on Rigid Substrates

The schematic illustration in **Figure 1** gives a general overview of the method used to form the $Au@SiO_2$-$CuIn(S,Se)_2$ absorber layer and solar cells. In brief, the $Au@SiO_2$ and $CuInS_2$ NPs were prepared separately following methods described in Section 4 (Figure 1). They were then mixed and deposited by drop casting on Mo/soda lime glasses (Mo/SLG). A selenization process was conducted to form the $Au@SiO_2$-$CuIn(S,Se)_2$ absorber layer, followed by the deposition of CdS buffer layers and i-ZnO/ITO transparent window layers (details in Section 4). For the $Au@SiO_2$ NPs preparation, citrate stabilized Au NPs with a diameter of approximately $≈17\,nm$ were used as the core while the SiO_2 shells with different thicknesses of 4, 6, and 17 nm were achieved using the Stöber process.[27] The transmission electron microscopy (TEM) image (Figure S1a, Supporting Information) shows a full device configuration,
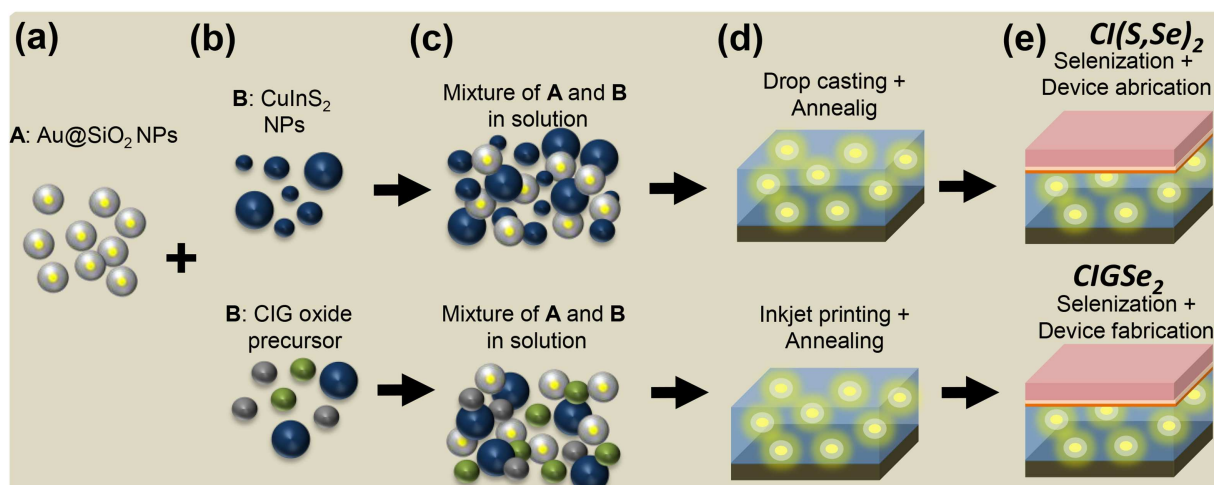

Figure 1. Schematic diagram of material preparation and device fabrication process. a)–c) $Au@SiO_2$ core-shell and $CuInS_2$ nanoparticles/CIG oxide precursor were prepared separately (see Section 4) then mixed to form a precursor solution according to optimized ratios for film formation. d) The precursor solution was then deposited by drop casting/inkjet printing followed by e) a high temperature selenization process and deposition of CdS/i-ZnO/ITO layers to form $CuIn(S,Se)_2$ and $Cu(In,Ga)Se_2$ solar cells, respectively.

containing the aggregated Au@SiO₂ NPs in the absorber layer, which can highly enhance the device absorption by the scattering effect.[28,29] The compositional mapping images of the observed Au@SiO₂ NPs were measured by energy-dispersive X-ray spectroscopy (EDS), confirming strong Au and Si signals in the core and shell regions (Figure S1b–d, Supporting Information).

To shed light on how the shell thickness affects the intrinsic plasmonic absorption by Au NPs, the different shell thicknesses were altered by changing the tetraethyl orthosilicate (TEOS) concentrations. The TEM image in **Figure 2**a shows a cluster of the uncoated Au cores with an average size of ≈17 nm. In Figure 2b–d, we can observe the Au@SiO₂ NPs with an increase in the thickness of the SiO₂ shell, confirming a homogeneous coating surrounding Au NPs. Figure S2, Supporting Information, shows the relationship between the TEOS concentrations used during the deposition process and the shell thickness. The distribution diagrams of varied shell thicknesses indicate the shell thickness ranging from 3.1 to 5.1, 5.4 to 7.7, and 15.3 to 19.3 nm in the case of 4, 6, and 17 nm, respectively. Since SPR peaks are sensitive to their surrounding medium, the Au@SiO₂

NPs are expected to have different plasmonic resonances wavelengths compared to pure Au NPs. Therefore, to assess the effect of the shell and its thickness on the SPR peak wavelength, we dispersed pristine Au NPs and Au@SiO₂ NPs with different shell thicknesses in ethanol solution for UV–Vis absorbance measurements as shown in Figure 2e. A small red-shift in SPR peaks can be observed, which are commonly attributed to the difference in the refractive index of silica that is slightly higher than that of its surrounding medium, i.e., ethanol.[30] Interestingly, Au@SiO₂ NPs have the SPR peak around 550 nm, the most intense wavelength of the AM 1.5 G solar spectrum. To ensure a homogeneous absorber layer after the addition of Au@SiO₂ NPs, a range of Au@SiO₂/CuInS₂ solutions with different concentrations calculated by per million over weight, i.e., Au@SiO₂/(Au@SiO₂ + CuInS₂) were prepared. These solutions were then deposited onto Mo substrates and subjected to the standard selenization process used for device fabrication. Subsequently, the films were examined via optical microscopy (OM) and absorbance spectrometer as shown in Figure S3, Supporting Information. In Figure S3a–f, Supporting Information, we can observe that at the concentrations of 84 ppm and above, a significant cracking behavior occurs while the continuous film images at concentrations of 0 ppm and 50 ppm are confirmed. The corresponding SEM images are also shown in Figure S3g–j, Supporting Information, respectively. In Figure S3k, Supporting Information, the enhancement factor (F_{Abs}) of absorbance, which is defined as the ratio of absorbance$_{with\ 50\ ppm\ Au@SiO2\ NPs}$/absorbance $_{Pristine}$, shows the broadband absorbance enhancement because of the scattering effect resulted from the aggregation of Au@SiO₂ NPs.[28,29] The severe fluctuation of F_{Abs} located around at 850 nm is due to oscillated signals resulted from switching of detector during the UV measurements. In addition, no change from the surface morphology in both cases can be observed (Figure S3g–j, Supporting Information), confirming that that the enhanced F_{Abs} is mainly caused by the Au@SiO₂ NPs.

One of the main hindrances toward the development of plasmonic-enhanced chalcopyrite solar cells is the high reactivity between Au and In/Cu/Ga once annealing temperatures above room temperature. To ensure the SiO₂ shell that provides sufficient protection to achieve the stable existence of Au NPs in the chalcopyrite absorber layer during the high-temperature selenization process, the as-synthesized Au@SiO₂ NPs were tested for thermal stability before and after addition of Au@SiO₂ NPs in CuIn(S,Se)₂ layer. First, our Au@SiO₂ NPs were heated to 600 °C for 1 h under an ambient environment. Figures 3a,b shows SEM images of the same core-shell NPs before and after heat treatment at the annealing temperature of 600 °C, respectively. Clearly, the SiO₂ shell remains stable and intact. Figure S4a,b, Supporting Information, shows TEM images of Au@SiO₂ NPs with the thinner shell thickness before and after the heat treatment at 600 °C for 1 h and the SiO₂ shell remains because of the high-melting point of the SiO₂ (1713 °C). Furthermore, we performed the selenization process at 600 °C on three films for ≈37 min, including pristine CuIn(S,Se)₂, Au-CuIn(S,Se)₂, and Au@SiO₂-CuIn(S,Se)₂, respectively. **Figure 3**c–h shows SEM images for the three respective films after the selenization process. In Figure 3c,d, the grain growth of the pristine CuIn(S,Se)₂ film can be observed as the typical
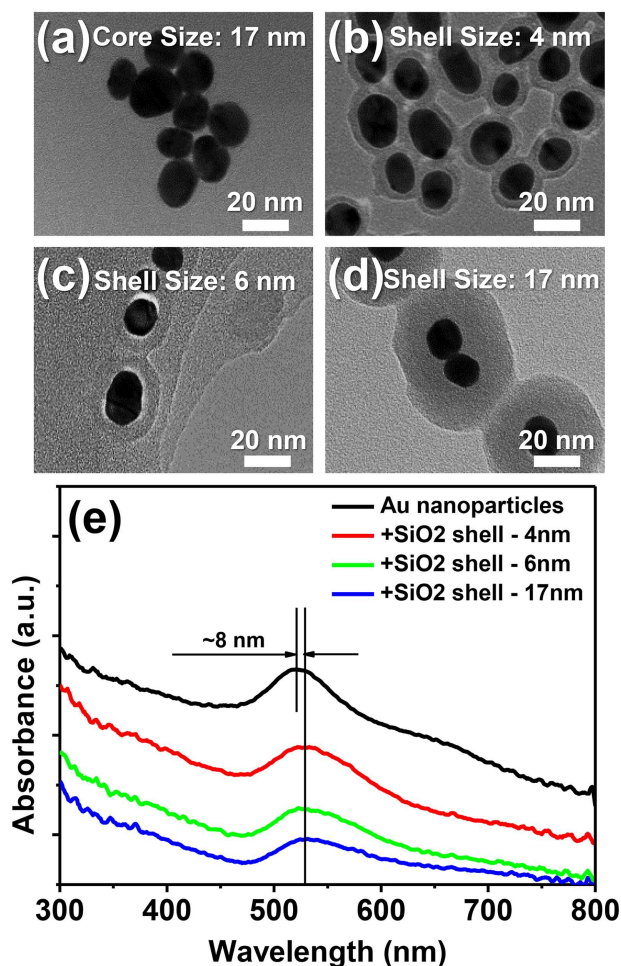
Figure 2. a) A HR-TEM images of an Au NP, HR-TEM images of Au NPs with b) 4 nm, c) 6 nm, and d) 17 nm-thick SiO₂ shell layers. e) Absorbance measurements of Au and Au@SiO₂ core-shell NPs.
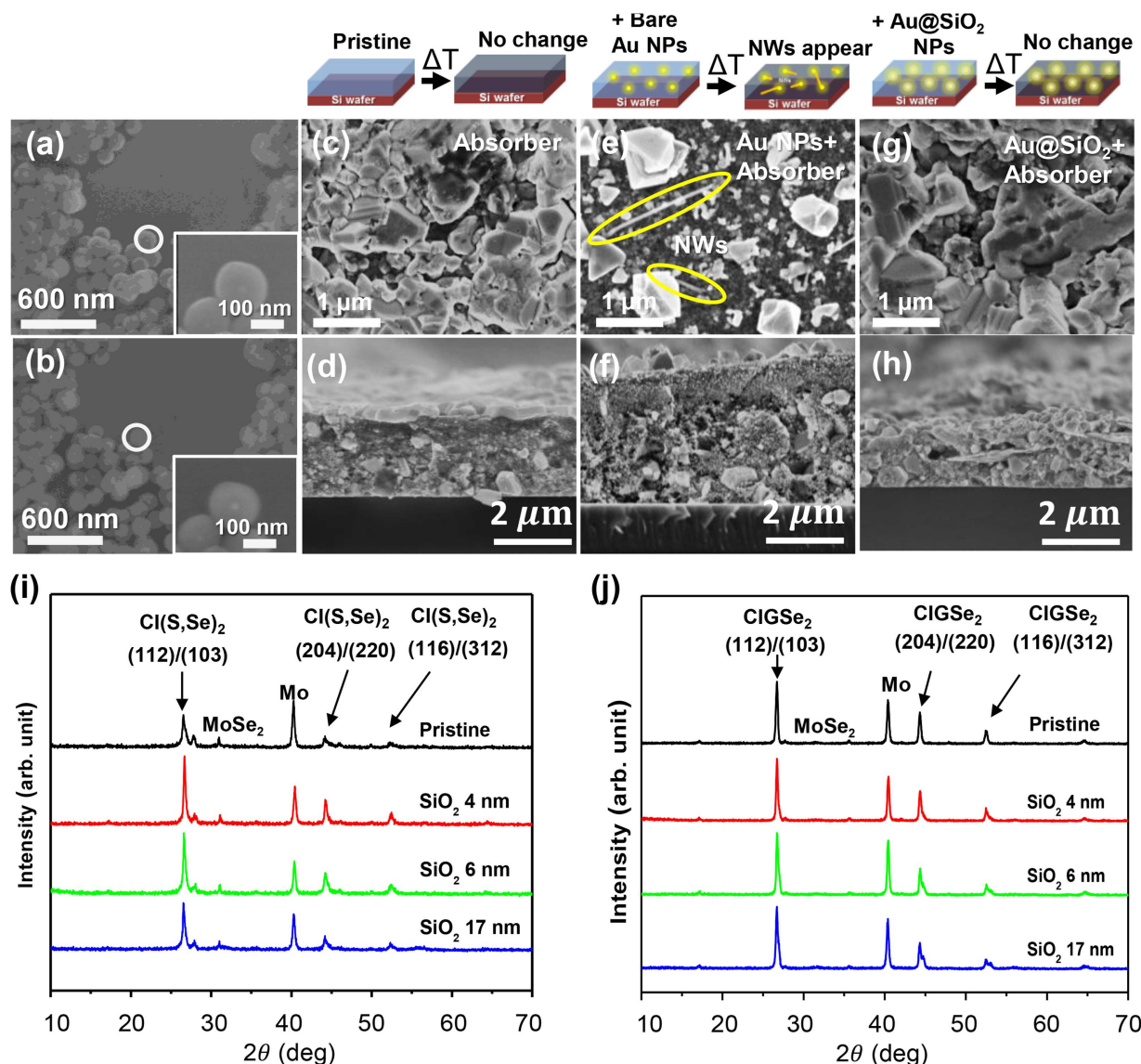
Figure 3. SEM images of Au@SiO$_2$ core-shell NPs a) before and b) after a thermal annealing process at the temperature of 600 °C. Plane-view and cross-section SEM images of the CuIn(S,Se)$_2$ absorber layer after the selenization process: c) and d) pristine CuIn(S,Se)$_2$ films, e) and f) CuIn(S,Se)$_2$ films with bare Au NPs, and g) and h) CuIn(S,Se)$_2$ films with Au@SiO$_2$ core-shell NPs. XRD spectra of i) pristine CuIn(S,Se)$_2$ films and j) pristine Cu(In,Ga)Se$_2$ films with and without the Au@SiO$_2$ core-shell NPs at different thicknesses.

reference. However, for the Au-CuIn(S,Se)$_2$ film, the formation of nanowires can be observed as shown in Figure 3e,f where the unprotected Au NPs act as catalysts. These nanowires can create shunting paths in the solar cell structure, leading to poor performance. Conversely, for Au NPs encapsulated by the SiO$_2$ shell layer after the selenization process as shown in Figure 3g,h, no NWs can be found and the film grain growth appears to be similar to the pristine CuIn(S,Se)$_2$ films, confirming that the SiO$_2$ shell layer offers sufficient protection to the Au NPs during the selenization process. The XRD spectra of the selenized pristine chalcopyrite films and chalcopyrite films after adding three different shell thicknesses of Au@SiO$_2$ NPs are shown in Figure 3i,j. The diffraction peaks can be referenced to (112, 103), (204, 220), and (116, 312), which are consistent with CuIn(S,Se)$_2$

and Cu(In,Ga)Se$_2$ planes. Two additional diffraction peaks can be observed at ≈30° and 40.2°, corresponding to MoSe$_2$ and Mo, respectively. Importantly, no diffraction peaks related to unwanted phases were found, confirming the excellent quality of the absorber layer after the post-selenization process.

Figure 4a–d shows the statistical device parameters extracted from current-density versus voltage (J–V) characteristics of pristine CuIn(S,Se)$_2$ and CuIn(S,Se)$_2$ solar cells after the addition of Au@SiO$_2$ NPs with three different SiO$_2$ shell thicknesses where the actual cell area of 0.3 cm^2 was used, respectively. V_{OC} values remain to be relatively unchanged while a little deviation in V_{OC} can still be observed across all devices. In addition, J_{SC} and corresponding FF were observed to be increased after the addition of the Au@SiO$_2$ NPs in the absorber
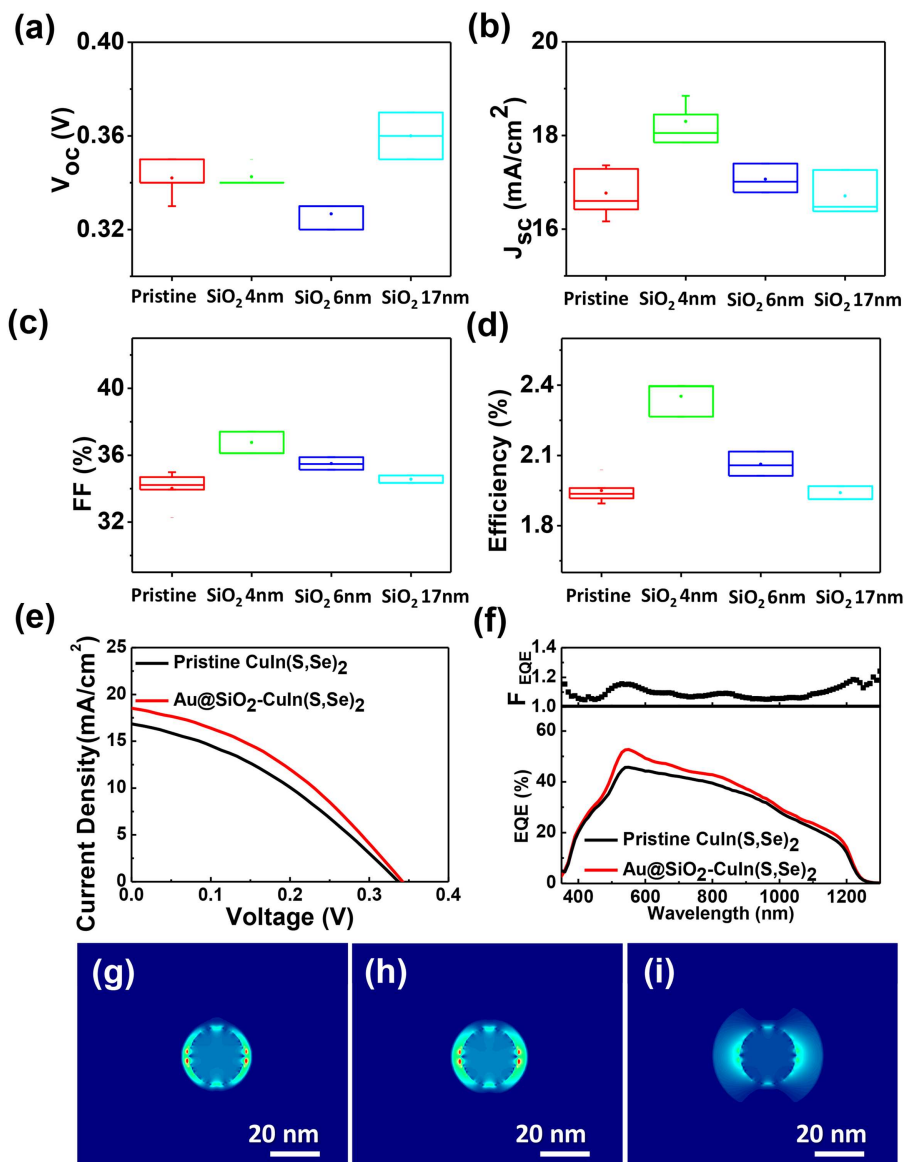
Figure 4. Box plots of extracted device parameters at a) open circuit voltage, b) short circuit current density, c) fill factor, and d) power conversion efficiencies for pristine CuIn(S,Se)$_2$ and Au@SiO$_2$-CuIn(S,Se)$_2$ solar cells with different thicknesses of SiO$_2$ shell layers, respectively. e) Typical current-density versus voltage plots for pristine CuIn(S,Se)$_2$ and Au@SiO$_2$-CuIn(S,Se)$_2$ solar cells with the SiO$_2$ thickness of 4 nm. f) The corresponding external quantum efficiency measurements and the enhancement factor. Three-dimensional finite difference time domain (FDTD) simulation results using Au NP in diameter of 17 nm with the SiO$_2$ shell thicknesses of g) 4, h) 6, and i) 17 nm under an incident light wavelength of 550 nm.

layer. In particular, we observed an increase in solar cell performance as the SiO$_2$ shell thickness decreases to 4 nm, providing the best performance in average. Figure 4e,f shows typical *J–V* characteristics and external quantum efficiency (EQE) results for both pristine and CuIn(S,Se)$_2$ solar cells after the addition of Au@SiO$_2$ NPs with the optimized SiO$_2$ shell thickness of 4 nm. These solar cells show an average of ≈9.12% enhancement in J_{SC} corresponding to ≈15.9% enhancement in PCE (from 1.95 to 2.26%). From the EQE measurements in Figure 4f, the broad and significant enhancement was achieved in the absorption properties of the solar cell, ranging from ≈500 nm to the cut-off region of the infrared bandgap. The

enhanced solar cell performance can be expected by two factors. First, we believe that the improvement of the light absorption and charge carrier generation at ≈550 nm, which can be observed in the enhancement factor of EQE (F_{EQE}) calculated by the ratio of EQE$_{with\ Au@SiO_2\ NPs}$/EQE$_{Pristine}$, is due to the excited localized surface plasmons on the Au NP. As the SPR-induced field is normally on the order of a few nanometers, we believe that the thinner shell enables better coupling behavior into the surrounding CuIn(S,Se)$_2$ absorption medium, increasing its effectiveness at light absorption to generate more charge carriers. Conversely, the thicker shell reduces coupling behavior into the CuIn(S,Se)$_2$, leading to the reduced device performance,

which is in good agreement with our results presented here. Second, the increased scattering from the Au NPs leads to an increase in the optical path length, resulting in improvement of charge carrier generation in the longer wavelengths (EQE measurements in Figure 4f). In order to clarify the effect of different SiO_2 shell thicknesses on the plasmonic field intensity, we performed three-dimensional finite difference time domain (FDTD) simulations on structures comprised of 17 nm Au NPs in diameter with SiO_2 shell thicknesses of 4, 6, and 17 nm under incident wavelengths of 550 nm where the refractive index values for Au NPs, SiO_2, and $CuIn(S,Se)_2$ were taken from the literature as discussed in Section 4. Figure 4g–i shows the spatial distribution of the square of electric field intensity ($|E|^2$) for each SiO_2 shell thickness. For each wavelength of incident light, there is a plasmonic response and the highest intensity of the enhanced localized electric field is observably stronger as the SiO_2 shell thickness decreases. This is in reasonable agreement with our optical absorption measurements shown in Figure 2e. Hence, we believe that the reduction in the shell thickness plays a crucial role in charge carrier generation, in turn leading to the enhancement in the J_{SC} and outright PCE observed in our solar cell devices.

2.2. Plasmonic Enhanced Au@SiO$_2$-Cu(In,Ga)Se$_2$ Solar Cells on Flexible Substrates

Furthermore, the addition of Au@SiO$_2$ NPs in Cu(In,Ga)Se$_2$-based solar cells fabricated on flexible substrates using an inkjet printing process was demonstrated. The detailed device fabrication processes were addressed in the experimental section. Briefly, CuO, In$_2$O$_3$, and Ga$_2$O$_3$ NP-based inks were printed on stainless steel (SS)/Cr/Mo substrates, followed by reduction process of the oxides in a hydrogen environment and a selenization process to form the final Cu(In,Ga)Se$_2$ absorber layer. Here, Au@SiO$_2$ NPs with 4 nm-thick SiO$_2$ shell was used because of the best enhancement observed in the CuIn(S,Se)$_2$ solar cells in the previous case. **Figure 5**a–c shows typical J–V characteristics, EQE measurements and an optical image of the Au@SiO$_2$-Cu(In,Ga)Se$_2$ device fabricated on the flexible stainless steel substrate, respectively. **Table 1** summarizes the extracted average values for open circuit voltage (V$_{OC}$), short circuit current (J$_{SC}$), fill factor (FF), and conversion efficiency (η). The actual cell area of 0.12 cm^2 was used. A significant increase in the J$_{SC}$ from 34.61 mA cm^{-2} to 35.94 mA cm^{-2}, corresponding to an increase in PCE from 9.28 to 10.88%, can be observed. On the other hand, the enhanced V$_{OC}$ and FF could be ascribed to the reduced bulk recombination by the SPR-induced strong near-field by Au@SiO$_2$ NPs,[31,32] which is confirmed by the enhanced intensity of photoluminescence (PL) signal in Figure S5, Supporting Information. Similarly to the EQE results obtained for the CuIn(S,Se)$_2$ solar cells shown in Figure 4f, Figure 5b shows a broad enhancement in charge carrier generation which can be plotted (F$_{EQE}$). Clearly, the enhanced F$_{EQE}$ in the region of 400–500 nm is due to the different CdS thicknesses and the improvement in the region of 500–600 nm can be attributed by the SPR absorption. From this enhanced charge carrier generation in the longer wavelengths, which is attributed by the scattering effect associated with the strong SPR
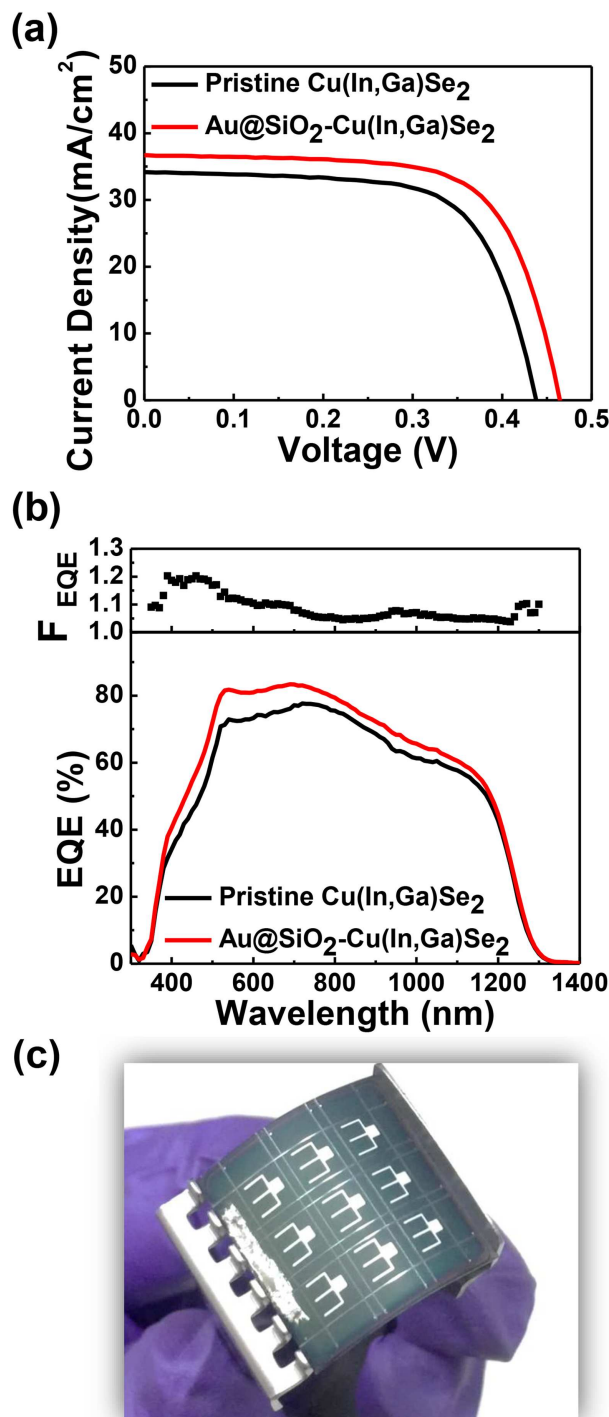
(a)

(b)

(c)

Figure 5. a) Typical current-density versus voltage plots for pristine Cu(In, Ga)Se$_2$ and Au@SiO$_2$-Cu(In,Ga)Se$_2$ with the SiO$_2$ thickness of 4 nm solar cells prepared by the inkjet-printed process. b) The corresponding external quantum efficiency measurements with the enhancement factor. c) An optical image of flexible Au@SiO$_2$-Cu(In,Ga)Se$_2$ solar cell with 3 × 3 patterned devices with Al top electrodes.

Table 1. The average device performance of $Cu(In,Ga)Se_2$ solar cells fabricated on flexible stainless steel substrates.

	V_{OC} [V]	J_{SC} [mA cm^{-2}]	FF [%]	η [%]
$Cu(In,Ga)Se_2$	0.43	34.61	62.64	9.28
$Cu(In,Ga)Se_2 + Au@SiO_2$ 4 nm	0.45	35.94	67.67	10.88

absorption peak observed at ≈ 550 nm, we believe that the addition of the $Au@SiO_2$ NPs offers the same two-fold benefit to our solar cells as observed in the $CuIn(S,Se)_2$.

3. Conclusions

In summary, we have demonstrated a facile method for the fabrication of $Au@SiO_2$ NPs toward solution-processed plasmonic-enhanced $Au@SiO_2$ NPs-$CuIn(S,Se)_2$ and $Au@SiO_2$ NPs-$Cu(In,Ga)Se_2$ solar cells, offering a significant enhancement in their light absorption and charge carrier generation properties. UV–Vis absorbance measurements show a small red-shift in the SPR related peak for the $Au@SiO_2$ NPs when compared to the Au particles and may be beneficial as the shift toward the 550 nm wavelength, the most intense wavelength of the AM 1.5 G solar spectrum. The thermal stability of our $Au@SiO_2$ NPs has been assessed using SEM and HR-TEM, confirming that the SiO_2 provides a protective layer to the Au NPs at high processing temperatures ($\approx 600\,^\circ$C) during the selenization process. The best solar cell performance can be obtained from devices for Au NPs covered by a 4 nm-thick SiO_2 shell, allowing better coupling between the SPR-induced field surrounding the absorption medium, thus improving absorption and charge carrier generation. The mechanism is in agreement with the FDTD simulation at different thicknesses of SiO_2 shell at the wavelength of 550 nm. EQE measurements confirm a spectrally broad enhancement in charge carrier generation for devices after the addition of $Au@SiO_2$ NPs at the SPR wavelength toward the cut-off region of the infrared bandgap. Enhanced power conversion efficiency in solution-processed rigid $CuIn(S,Se)_2$ from 1.95 to 2.26% and flexible $Cu(In,Ga)Se_2$ solar cells from 9.28 to 10.88% can be achieved after adding of plasmonic Au-SiO_2 core-shell NPs in the absorber layer due to both the plasmonic coupling and increased scattering.

4. Experimental Section

Synthesis of Au@SiO$_2$ Nanoparticles: Au NPs were obtained using a commonly applied method first demonstrated by Turkevitch in 1951 where $HAuCl_4$ is reduced and stabilized by sodium citrate.[33] 50 ml of 1 mM $HAuCl_4$·$3H_2O$ solution was prepared and boiled under reflux and vigorous stirring. Subsequently, 5 mL 18.8 mM of sodium citrate was added to the solution, resulting in a color change from yellow to wine-red, confirming the formation of Au NPs. In this work, Au NPs with an average diameter of ≈ 17 nm were formed. The silica shell was formed using the Stöber method where the TEOS was used as the precursor.[27] The reaction takes place spontaneously by hydrolysis of silyl ethers to silanol followed by condensation. In brief, freshly prepared 4 mL PVP aqueous solution was added to 5 mL solution containing Au NPs, followed by 0.36 mL of 1 mM MHA dissolved in ethanol solution. After centrifugation,

the sediment was collected and 5 mL of 0.5 mM TEOS ethanol solution was added to the surface-modified gold solution, followed by sonication for ≈ 5 s. 1 mL of 28 wt% NH_4OH (to control the reaction rate) was then added under mild stirring. The resulting dispersion was then allowed to stand for 2 h so that the active silica can be polymerized on Au NPs. The particles can then be transferred into ethanol solution and stored in a refrigerator for further characterization. Under these conditions, a SiO_2 thickness of ≈ 4 nm can be achieved. However, the shell thickness of the SiO_2 can easily be altered by adjustment of the TEOS concentrations.

Fabrication of CuIn(S,Se)$_2$ Solar Cells on Ridged Substrates: Mo (400 nm) was deposited on soda lime glasses (SLG) as the back electrode using a two-stage sputtering process. $CuInS_2$ particles were fabricated using a non-vacuum process under N_2 where copper chloride, indium chloride, and polyamine precursors were mixed in a three neck bottle under the vigorous stirring at $130\,^\circ$C until they dissolved.[34] The reaction temperature was then raised to $200\,^\circ$C at a rate of $10\,^\circ$C min^{-1}, followed by the addition of sulfur powder for 30 min. The mixture is allowed to cool naturally, after which the $CuInS_2$ particles were recovered by centrifugation. The $Au@SiO_2$ NPs incorporated $CuIn(S,Se)_2$ film was fabricated by drop casting an $Au@SiO_2$-$CuInS_2$ NPs solution on Mo following by selenization at $600\,^\circ$C for 30 min. A CdS buffer layer was deposited by chemical bath deposition (CBD) process followed by i-ZnO and ITO by magnetron sputtering with thicknesses of 50 nm and 550 nm, respectively.

Fabrication of Cu(In,Ga)Se$_2$ Solar Cells on Flexible Substrates: The $Cu(In,Ga)Se_2$ absorber was fabricated using CuO, In_2O_3, and Ga_2O_3 NPs dispersed in deionized water as an ink and then printed onto stainless steel (SS)/Cr/Mo substrates where the sputtered Cr acts as a Fe diffusion blocking layer. The oxide precursors were reduced in a hydrogen atmosphere at $500\,^\circ$C to form a Cu–In–Ga alloy. The films were then subjected to a $500\,^\circ$C selenization process for 30 min.[35] A CdS buffer layer and i-ZnO, AZO window layer were then deposited by the same process used for the $CuIn(S,Se)_2$ film preparation.

Measurements, Characterizations, and FDTD Simulation: The morphologies and nanostructures of the various films and $Au@SiO_2$ NPs were assessed by field-emission scanning electron microscopy (FESEM by Hitachi, S-4000 and SU8000) and high-resolution transmission electron microscopy (HR-TEM by JEOL, JEM-3000F FEGTEM, 300 kV). Powder X-ray diffraction (XRD) was conducted using a Shimadzu XRD-6000 X-ray spectrometer under Cu-K_α ($\lambda \approx 1.54$ Å) irradiation. Absorbance spectroscopy was obtained using a U-4100 UV–Vis–NIR Spectrometer. PL was measured by a pulsed laser source (He–Ne laser 638 nm). The J–V characteristics was measured using a Keithley 4200 system under AM 1.5 solar illumination at room temperature. The EQE spectrum of the devices was carried out using a xenon lamp under 75 W, a monochromator and a lock-in amplifier. FDTD simulation was conducted using FDTD Solutions 8.0 software. The Au and SiO_2 shell size were set to 17 and 4 nm, 6 and 17 nm respectively. The refractive index values of Au NPs were taken from the "Au (Gold)-CRC" default material database, and that of $CuInSe_2$ was taken from a previous report by Paulson.[36]

Supporting Information

The TEM images of the full device containing $Au@SiO_2$ NPs, the relationship between the TEOS concentration and shell thickness, optical images of different concentration $Au@SiO_2$-$CuIn(S,Se)_2$ mixtures deposited on Mo substrate, SEM images of the $CuIn(S,Se)_2$ surface morphology, the TEM images of the thermal stability test and PL spectra of the $Au@SiO_2$ embedded $Cu(In,Ga)Se_2$ film. Supporting Information is available from the Wiley Online Library or from the author.

Acknowledgements

Conflict of Interest

The authors declare no conflict of interest.

Keywords

core-shell nanoparticles, plasmonic solar cells, solution processes, thin film solar cells

[1] P. Spinelli, M. Hebbink, R. de Waele, L. Black, F. Lenzmann, A. Polman, *Nano Lett.* **2011**, *11*, 1760.

[2] P. Spinelli, V. E. Ferry, J. van de Groep, M. van Lare, M. A. Verschuuren, R. E. I. Schropp, H. A. Atwater, A. Polman, *J. Opt.* **2012**, *14*, 024002.

[3] K. R. Catchpole, A. Polman, *Opt. Express* **2008**, *16*, 21793.

[4] M. Geneviève, C. Vieu, R. Carles, A. Zwick, G. Brière, L. Salomé, E. Trévisiol, *Microelectron. Eng.* **2007**, *84*, 1710.

[5] T. Chung, S. Y. Lee, E. Y. Song, H. Chun, B. Lee, *Sensors* **2011**, *11*, 10907.

[6] S. J. Lee, Z. Guan, H. Xu, M. Moskovits, *J. Phys. Chem. C* **2007**, *111*, 17985.

[7] R. Adato, A. A. Yanik, J. J. Amsden, D. L. Kaplan, F. G. Omenetto, M. K. Hong, S. Erramilli, H. Altug, *Proc. Natl. Acad. Sci. U.S.A.* **2009**, *106*, 19227.

[8] A. J. Haes, C. L. Haynes, A. D. McFarland, G. C. Schatz, R. P. Van Duyne, S. Zou, *MRS Bull.* **2005**, *30*, 368.

[9] P. Reineck, G. P. Lee, D. Brick, M. Karg, P. Mulvaney, U. Bach, *Adv. Mater.* **2012**, *24*, 4750.

[10] J.-L. Wu, F.-C. Chen, Y.-S. Hsiao, F.-C. Chien, P. Chen, C.-H. Kuo, M. H. Huang, C.-S. Hsu, *ACS Nano* **2011**, *5*, 959.

[11] R. A. Pala, J. White, E. Barnard, J. Liu, M. L. Brongersma, *Adv. Mater.* **2009**, *21*, 3504.

[12] J. Yang, J. You, C.-C. Chen, W.-C. Hsu, H.-r. Tan, X. W. Zhang, Z. Hong, Y. Yang, *ACS Nano* **2011**, *5*, 6210.

[13] K. Jung, H.-J. Song, G. Lee, Y. Ko, K. Ahn, H. Choi, J. Y. Kim, K. Ha, J. Song, J.-K. Lee, C. Lee, M. Choi, *ACS Nano* **2014**, *8*, 2590.

[14] E. Stratakis, E. Kymakis, *Mater. Today* **2013**, *16*, 133.

[15] J. Wang, Y.-J. Lee, A. S. Chadha, J. Yi, M. L. Jespersen, J. J. Kelley, H. M. Nguyen, M. Nimmo, A. V. Malko, R. A. Vaia, W. Zhou, J. W. P. Hsu, *J. Phys. Chem. C* **2013**, *117*, 85.

[16] M. D. Brown, T. Suteewong, R. S. Kumar, V. D'Innocenzo, A. Petrozza, M. M. Lee, U. Wiesner, H. J. Snaith, *Nano Lett.* **2011**, *11*, 438.

[17] X. Luan, Y. Wang, *J. Mater. Sci. Technol.* **2014**, *30*, 1.

[18] C. Andrei, E. Lestini, S. Crosbie, C. de Frein, T. O'Reilly, D. Zerulla, *PLoS ONE* **2014**, *9*, e109836.

[19] V. E. Ferry, L. A. Sweatlock, D. Pacifici, H. A. Atwater, *Nano Lett.* **2008**, *8*, 4391.

[20] U. W. Paetzold, E. Moulin, D. Michaelis, W. Böttler, C. Wächter, V. Hagemann, M. Meier, R. Carius, U. Rau, *Appl. Phys. Lett.* **2011**, *99*, 181105.

[21] S. Pillai, K. R. Catchpole, T. Trupke, M. A. Green, *J. Appl. Phys.* **2007**, *101*, 093105.

[22] K.-C. Tseng, Y.-T. Yen, S. R. Thomas, H.-W. Tsai, C.-H. Hsu, W.-C. Tsai, C.-H. Shen, J.-M. Shieh, Z. M. Wang, Y.-L. Chueh, *Nanoscale* **2016**, *8*, 5181.

[23] W.-C. Tsai, S. R. Thomas, C.-H. Hsu, Y.-C. Huang, J.-Y. Tseng, T.-T. Wu, C.-h. Chang, Z. M. Wang, J.-M. Shieh, C.-H. Shen, Y.-L. Chueh, *J. Mater. Chem. A* **2016**, *4*, 6980.

[24] S. Thomas, C.-W. Chen, M. Kondiba, C.-Y. Wang, H.-W. Tsai, Z. Wang, Y.-L. Chueh, *RSC Adv.* **2016**, *6*, 60643.

[25] J.-L. Wu, Y. Hirai, T. Kato, H. Sugimoto, V. Bermudez, in *7th World Conference on Photovoltaic Energy Conversion (WCPEC-7)*, Waikoloa, HI, USA **2018**.

[26] H. A. Atwater, A. Polman, *Nat. Mater.* **2010**, *9*, 205.

[27] W. Stöber, A. Fink, E. Bohn, *J. Colloid Interface Sci.* **1968**, *26*, 62.

[28] H.-Y. Kim, W.-Y. Rho, H. Y. Lee, Y. S. Park, J. S. Suh, *SoEn* **2014**, *109*, 61.

[29] S. Nafiseh, D. Ali, D. Davood, T. Nima, *J. Opt.* **2016**, *18*, 015902.

[30] Y. Lu, Y. Yin, Z.-Y. Li, Y. Xia, *Nano Lett.* **2002**, *2*, 785.

[31] S.-C. Chen, K.-H. Wu, J.-X. Li, A. Yabushita, S.-H. Tang, C. W. Luo, J.-Y. Juang, H.-C. Kuo, Y.-L. Chueh, *Sci. Rep.* **2015**, *5*, 18354.

[32] S.-C. Chen, Y.-J. Chen, W. T. Chen, Y.-T. Yen, T. S. Kao, T.-Y. Chuang, Y.-K. Liao, K.-H. Wu, A. Yabushita, T.-P. Hsieh, M. D. B. Charlton, D. P. Tsai, H.-C. Kuo, Y.-L. Chueh, *ACS Nano* **2014**, *8*, 9341.

[33] J. Turkevich, P. C. Stevenson, J. Hillier, *Discuss. Faraday Soc.* **1951**, *11*, 55.

[34] M. G. Panthani, V. Akhavan, B. Goodfellow, J. P. Schmidtke, L. Dunn, A. Dodabalapur, P. F. Barbara, B. A. Korgel, *J. Am. Chem. Soc.* **2008**, *130*, 16770.

[35] L.-P. Wang, C.-C. Chiang, Y.-Y. Wang, T.-K. Yeh, W.-C. Chen, S.-Y. Tsai, *Surf. Coat. Technol.* **2013**, *231*, 590.

[36] P. D. Paulson, R. W. Birkmire, W. N. Shafarman, *J. Appl. Phys.* **2003**, *94*, 879.